PHYSICAL REVIEW FLUIDS **3**, 094803 (2018)

Editors' Suggestion

Geometrical focusing of surface waves

Gerardo Ruiz Chavarria[*]
Departamento de Fisica, Facultad de Ciencias, Universidad Nacional Autonoma de Mexico,
Ciudad Universitaria, 04510, Mexico

Patrice Le Gal and Michael Le Bars
CNRS, Aix Marseille Univ, Centrale Marseille, IRPHE, Marseille, 13013, France

(Received 15 May 2018; published 5 September 2018)

In this paper we investigate experimentally the waves produced by a parabolically shaped wave maker partially immersed into a water-filled basin and oscillating in the vertical direction. The main motivation of our study is to follow the analogy between light waves that focus on caustics, creating zones of intense light concentration, and surface waves in liquids. Similarly to light focusing, the surface waves undergo spatial focusing leading to the growth of their amplitudes till they reach a cusp singularity. We detect three regimes. In the first one, which corresponds to small forcing amplitudes, the wave field agrees well with geometrical optics and with Pearcey diffraction theory near the caustics. In the second regime, weak nonlinearities are detected. However, waves still focus as predicted. In the third regime, at large forcing amplitude, a large-scale mean flow is generated. This flow is concentrated in two symmetric jets emerging from the wave maker front wall and producing two counter-rotating eddies because of the finite size of the basin. This large-scale flow modifies the shape of the wave fronts and leads to a displacement of the cusp towards the wave maker, modifying the analogy between light and surface waves.

DOI: 10.1103/PhysRevFluids.3.094803

I. INTRODUCTION

Waves are ubiquitous in every day life. Two common examples are light and sound, but the best-known illustration of traveling waves is certainly the circular wave pattern propagating on the free surface when a stone is thrown in water. The theory of surface waves in liquids is based on the assumptions that the flow is inviscid and nonrotational. When small amplitude is assumed for the waves, the quadratic term in the Bernoulli equation can be neglected, and the linear dispersion relation of surface waves is obtained:

$$\omega^2 = \left(gk + \frac{\sigma k^3}{\rho}\right)\tanh(kH), \tag{1}$$

where ω is the wave frequency, k their wave number, ρ the liquid density, σ the surface tension coefficient, g the gravity acceleration, and H the depth of the liquid layer. In the limit of deep water ($kH \gg 1$) the waves are dispersive, that is, their phase velocity depends on their wavelength. On the opposite limit ($kH \ll 1$), known as the shallow water approximation, the phase velocity is equal to $\sqrt{gH}$ irrespective of the magnitude of the wavelength. The usual picture for a wave profile is a sinusoidal function, which is valid for linear waves. But, when the quadratic term of the Bernoulli equation is taken into account (but small wave amplitude compared to water depth is still retained),

---

[*] gruiz@unam.mx

new behaviors appear. For example, some asymmetries in the vertical direction appear (the troughs are rounded and the crests become sharp), and the phase velocity exhibits a slight dependency on the wave amplitude. Furthermore, waves of finite amplitude cannot grow indefinitely, and there is a threshold in steepness above which they break [1], transferring energy to capillary waves, bubbles, and turbulence [2,3]. Oceanic waves play a major role in the atmosphere-ocean balance [4], and it is a major issue in oceanography to know the mechanisms for the production and the dissipation of energy by waves, but also to quantify the transfer of mass and momentum between air and water.

The question about the condition for a wave to break is still open even if some efforts have been made to establish dynamical or kinematical criteria for the appearance of wave breaking [1]. For instance, when a wave has components of different frequencies, the superimposition of these components at some point in space and time could lead to the growth of the wave amplitude beyond the aforementioned threshold [5,6]. A good method to study wave breaking, based on the work of Longuet-Higgins [7], is to use temporal focusing due to the dependence of the group velocity upon the frequency. A little more sophisticated method has been used by Rapp and Melville [8]. They produce a wave train containing 32 components of equal amplitude, all focusing at a given point for a precalculated time. In this manner, the sum of the 32 components leads to a breaking wave at the point of focusing.

Here we study the geometrical focusing of water waves generated by a parabolic-shaped wave maker. The growth of the wave slope is less than those obtained by Rapp and Melville [8] using temporal focusing. However, focusing occurs for all time in our setup, which may be an advantage in exploring wave breaking, as expected for future studies. This focalization process has already been evoked for the formation of rogue waves in the ocean [6,9]. The ultimate goal of our study will be to tackle some aspects of the breaking wave problem in the laboratory on a rather small facility. As a first step, we present in this article the analogy of our hydrodynamical system with the focusing of light in a cusp [10]. As already mentioned, if the waves have a small amplitude, the inherent nonlinear properties of their propagation might not break the analogy with light. In this case, surface waves focus as expected, following the ray theory of geometrical optics or, if we take into account diffraction, the more sophisticated theory of Pearcey [11]. Then we will show that weak nonlinearity, even if it breaks the vertical symmetry of the waves (crests and troughs are no more symmetric), does not affect too much the theoretical prediction about focusing. On the contrary, this is no longer the case when the forcing amplitude is strong enough to generate a steady large-scale surface flow. This flow transports and deforms the waves and consequently moves the cusp much more closer to the wave maker than the predicted locations of the Huygens cusp.

The present article is organized as follow: in Sec. II we describe the basic principles of geometrical optics, and we give some details of the rays and wave fronts produced by a parabolic wave maker. In Sec. III the experimental setup, the methods to study surface waves, and velocity on the free surface are given. In Sec. IV the results of wave properties and focusing are described. Three different subsections present, respectively, the small amplitude, the medium amplitude, and the large amplitude wave focusing properties. In the case of medium amplitude the nonlinear effects are highlighted, in particular the asymmetry of the wave profile. In the case of large amplitude, the properties and the effects of large-scale surface flows are presented. Finally in Sec. V some conclusions and perspectives are drawn.

II. GEOMETRICAL OPTICS

Two concepts underlie geometrical optics: “rays” and “wave fronts.” A ray is a line along which a wave propagates, while a wave front is a line of constant phase, which can be constructed as a curve perpendicular to rays. In our study, the water surface is disturbed with an oscillating parabolic wave maker [12,13]. To trace a ray we need the normal vector in all points of the parabola. If the equation of the parabola reads

$$y_0 = ax_0^2, \tag{2}$$

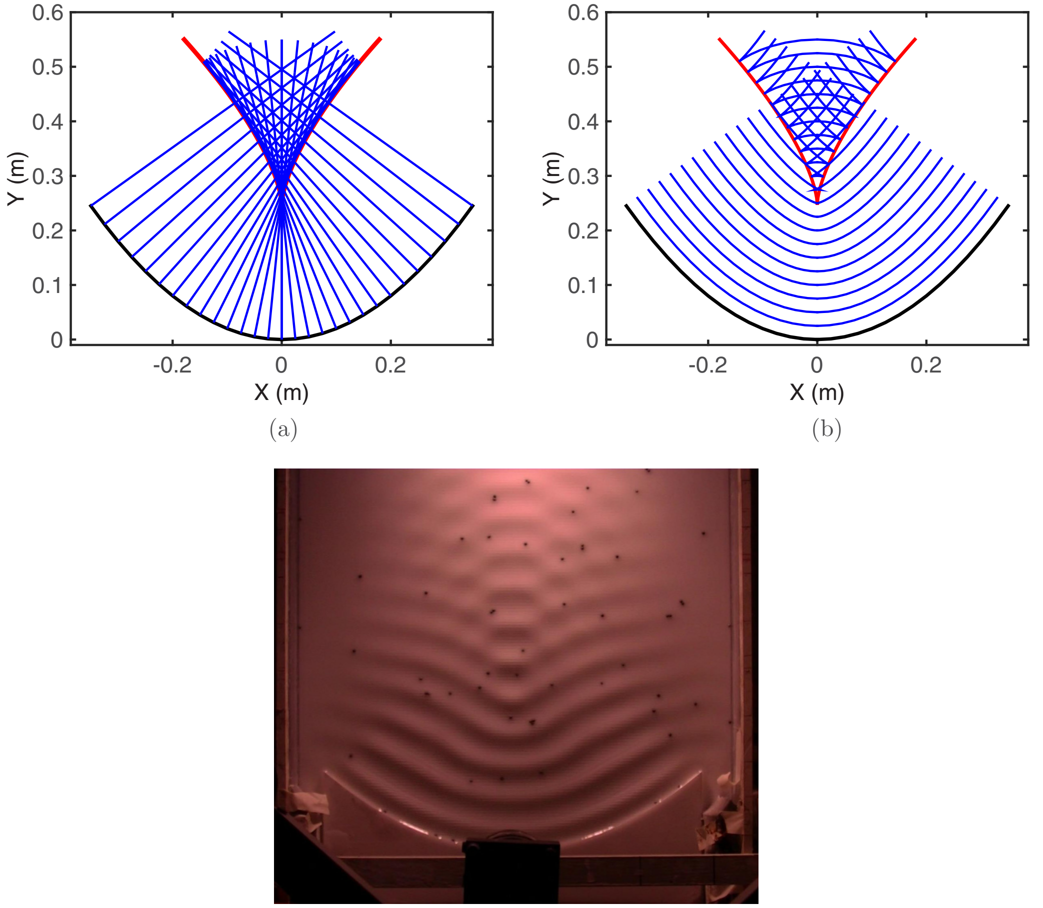

(a)

(b)

(c)

FIG. 1. Rays and wave fronts produced by a parabolic wave maker as predicted by geometrical optics. (a) Rays starting at each point (x_0, y_0) of the parabolic wave maker following the normal to the parabola. (b) Wave fronts produced by the parabolic wave maker. They are perpendicular to rays and move towards the top. (c) Picture of the wave maker, the basin, and the shaker. The wave field is visualized by adding white concentrated ink to water. The black dots are small floating beads used to measure the mean surface flow by particle tracking.

then the normal vector at any initial location is $\hat{\mathbf{n}} = \frac{(1, -2ax_0)}{\sqrt{(1+4a^2x_0^2)}}$. Consequently any position (x, y) on a ray starting at point (x_0, y_0) obeys the following equation:

$$(x, y) = (x_0, y_0) + \frac{(1, -2ax_0)}{\sqrt{\left(1 + 4a^2x_0^2\right)}} c\, t, \tag{3}$$

where c is the phase speed of the waves and t is the time. The product $c\,t$ is the distance d traveled by a front along a ray from its starting point (x_0, y_0). In Fig. 1 we show both rays and wave fronts emitted by the parabolic wave maker as they are predicted by the geometrical optics. Rays are obtained from Eq. (3) leaving x_0 constant and varying t, whereas wave fronts are recovered leaving t constant and varying x_0. In Sec. IV we will compare experimental wave fronts with those predicted by geometrical optics.

According to geometrical optics, rays starting at point (x_0, y_0) converge to the curvature center of the wave fronts, which can be calculated as a function of (x_0, y_0). The curvature κ can be calculated as usual for a planar curve:

$$\kappa = \frac{\frac{d^2 y_0}{dx_0^2}}{\left[1 + \left(\frac{dy_0}{dx_0}\right)^2\right]^{3/2}}. \tag{4}$$

From this formula the radius of curvature is simply $\rho = 1/\kappa$. As energy is conserved along a ray (dissipation is small and neglected), we can deduce that the amplitude η of a wave at any arbitrary point satisfies

$$\eta = \eta_0 \sqrt{\frac{\rho}{\rho - d}}, \tag{5}$$

where d is the distance traveled by a ray from a starting point (x_0, y_0) at the parabolic wave maker and η_0 the wave initial amplitude. As can be seen in Eq. (5), the amplitude of the wave field should diverge according to the ray theory at points where $d = \rho$. For instance along the symmetry axis ($x = 0$), the greatest amplitudes are attained for $d = \rho = 1/2a$. This point $(0, \frac{1}{2a})$ of singular behavior for the wave field is the summit of a cusp called the Huygens cusp. The wave field exhibits also the existence of two caustics that merge at the summit of the Huygens cusp. The primary definition of a caustics is a region (a line in two-dimensional wave fields and a surface for three-dimensional waves) where, according to the ray theory, wave amplitude becomes infinite. Using Eqs. (2)–(5), we determine the equation for these two caustics:

$$x = \pm \frac{4}{3}\sqrt{\frac{a}{3}}\left(y - \frac{1}{2a}\right)^{3/2}. \tag{6}$$

Caustics are also the loci where wave fronts fold, i.e., where there is a change in the sign of the curvature of the waves fronts. Because of the divergence of the rays, wave amplitude is expected to decrease after a caustics. Note also that if we reintroduce the oscillatory behavior of waves, diffraction and interference are expected to be produced by the superimposition of more than one ray. Therefore, ray theory breaks down if we consider spatial scales shorter than the wavelength as it is the case for nearby caustics. In the 19th century, Airy developed a theory to describe the behavior of waves near simple caustics [14]. He constructed a function having an oscillatory behavior in one domain and an exponential decay in another one with the intention to reproduce the features of the wave envelopes on both sides of caustics. However, Airy's theory does not apply in the neighborhood of the cusp, as three rays intersect there and not only two. Instead, we use a diffraction integral as done in the pioneering work of Pearcey [11]. This is an approximate solution which does not diverge at caustics and thus allows us to determine the behavior of linear waves around those. The wave field is approximated by the following integral that simply represents the summation of all initial point source contributions along the wave maker:

$$\eta(x, y) = \int_{-\infty}^{+\infty} \frac{\exp[ikd(x_0, x, y)]}{\sqrt{d(x_0, x, y)}} \frac{dx_0}{\cos[\theta(x_0)]}, \tag{7}$$

where d is as before the distance from point (x, y) to the parabola, $\cos[\theta(x_0)]$ the angle of the rays versus the symmetric axis of the parabola, and k the wave number of the considered wave. Because our interest is to describe the wave field in the vicinity of the singularity, we perform a Taylor expansion of the length d around the Huygens cusp summit $(0, \frac{1}{2a})$. We use this expansion only in the term $kd(x_0, x, y)$ inside the exponential, whereas in the denominator we use the approximation $d \approx \frac{1}{2a}$. The final result is known as the Pearcey integral [11]:

$$\eta(x, y) = \frac{k}{i2\pi} \frac{\exp(ikR)}{\sqrt{R}} \left(\frac{2R}{ka^2}\right)^{1/4} \int_{-\infty}^{+\infty} \exp(i[s^4 + Us^2 + Vs])ds, \tag{8}$$

where $R = \frac{1}{2a}$, $U = 2(\frac{k}{2R})^{\frac{1}{2}}(R - y)$, $V = -\frac{2}{\sqrt{a}}(\frac{k}{2R})^{\frac{3}{4}}x$, and $s = (\frac{ka^2}{2R})^{\frac{1}{4}}x_0$.

The calculation of the Pearcey integral will be used later to compare its predictions with our experimental results. We must remark that the wave maker has a finite size, so to make a correct comparison with the experiments, the limits in the previous integral must be replaced by finite values.

III. EXPERIMENTAL SETUP

Our experiments involve the measurements of both the topography of the oscillating free surface and the velocity field on this surface. To investigate the wave fields, we use two methods developed in the last decade: the synthetic Schlieren method [15] and the Fourier transform profilometry [16] (FTP). Both methods have been developed on the basis of the use of digital cameras. The first method is based on light refraction. To implement it, a pattern of dots randomly distributed is placed at the bottom of the transparent liquid layer. When a surface wave travels, it induces an apparent displacement $\delta\overrightarrow{r}$ of each dot, related to the gradient of the free surface deformation through a linear relation:

$$\nabla\eta = -\frac{\delta\overrightarrow{r}}{h^{*}}, \tag{9}$$

where $\frac{1}{h^{*}} = \frac{1}{\alpha H} - \frac{1}{L}$ with H the layer depth, L the distance from the camera to the liquid bottom, and α is related to the ratio of the refractive indices of, respectively, the liquid (n') and air (n): $\alpha = 1 - \frac{n'}{n}$. In an air-water interface $\alpha = 0.24$. To measure $\delta\overrightarrow{r}$, we use a PIV software; our choice was a free distribution software developed by Meunier and Leweke, DPIVsoft [17]. Finally to calculate η, we integrate Eq. (9) with a method of least squares because the system of equations is overdetermined. The synthetic Schlieren method works well for waves of small amplitudes; however, it is not suitable to studying high-amplitude nonlinear regimes. In this case, we use instead the FTP method, which is based on light reflection. To implement it, the liquid-air interface must be opaque to produce a diffuse reflection of light. For this purpose some concentrated white paint is added in the water. Among a great variety of paints we have chosen the dye that produces a small modification of water viscosity and surface tension [16]. A fringe pattern of a given spatial period p is then projected on the liquid surface by the use a high-definition video projector (1920 × 1080 pixels). In a second step the fringe pattern is recorded with a digital camera able to record frames with a depth of 16 bits per color. To reconstruct the free surface topography we need to take snapshots when the liquid surface is flat and then when it is deformed by the waves. These two images will be used to calculate the phase changes of the fringe pattern due to the presence of the waves. Among some possible technical configurations we use an arrangement where the camera and the projector have parallel axes. In this case, the relation between the deformation of the free surface and the phase difference $\Delta\phi$ is [16]

$$\eta = \frac{\Delta\phi L}{\Delta\phi - \frac{2\pi}{p} D}, \tag{10}$$

where L is the distance from the camera to the liquid surface and D the distance between the camera and the video projector lens.

The experiments using the synthetic Schlieren or FTP method were both carried out in a 1.2 m long, 0.5 m wide, and 0.15 m deep basin. The basin was filled with water up to 12.5 cm. To produce the waves, we used a parabolic wave maker with a geometric parameter $a = 2\ \mathrm{m}^{-1}$ and 42 cm wide. This wave generator plunges 2 mm into the water. In order to vibrate the wave maker, we connect it to a shaker which is excited with a power supply capable of generating monochromatic waves with frequencies in the range from 5 to 10 Hz. The initial amplitude of the waves is given by the amplitude of the forcing. Both were checked to be proportional to the voltage applied to the shaker at a chosen frequency. These excitations correspond to wavelengths lying between 2.3 and 6.6 cm with a phase speed between 23.2 and 33.1 cm/s. Under these conditions, the produced waves are capillary-gravity waves. The Huygens cusp is located 25 cm away from the parabola vertex, so the distance from the wave maker to the caustics is covered by several wavelengths. To avoid wave reflection some pieces

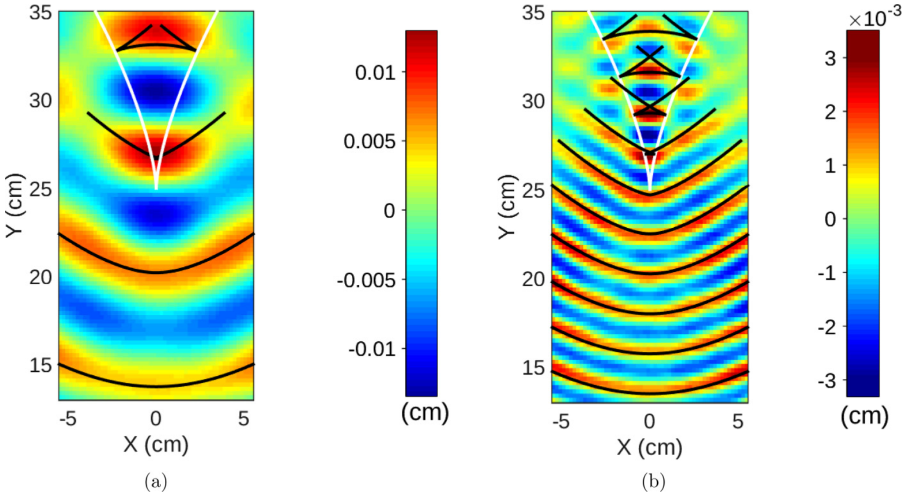

(a)

(b)

FIG. 2. Topography of the free surface measured with the synthetic Schlieren method for two frequencies: (a) $f = 5$ Hz and $\eta_0 = 36\ \mu$m, (b) $f = 10$ Hz and $\eta_0 = 8\ \mu$m. For comparison we draw also some wave fronts (black lines) as predicted by ray theory. These wave fronts are separated from each other by a wavelength λ. The waves have small amplitudes, so nonlinearities are weak. The shape of the wave fronts and the value of the wavelength λ agree very well, respectively, with the prediction of geometrical optics and the linear dispersion relation for surface waves [see Eqs. (3) and (1)]. In addition we also draw the caustics (white line).

of foam were disposed all along the lateral walls of the basin. As we will see in the following, we also measure the mean flow induced at the free surface in the case of large oscillation amplitudes. To measure the velocity field we tracked during 2 min for each run polystyrene floating particles that were randomly spread on the water surface.

IV. EXPERIMENTAL RESULTS

A. Small amplitude wave experiments: No evidence of nonlinear effects

The wave fields for small forcing amplitudes were investigated using the synthetic Schlieren method. In Fig. 2 we show the topography of the free surface for two frequencies of 5 and 10 Hz. The corresponding wavelengths are 6.6 cm and 2.3 cm, and their initial amplitudes are 36 μm and 8 μm. The area covered in the figure includes the region where spatial focusing occurs, the two caustics, and a region where the wave amplitude decreases.

In order to compare the experimental data with geometrical optics, we include in the figure some wave fronts as predicted by Eq. (3). The first one is superimposed to the experimental curve of maximal amplitude closest to the wave maker. The other wave fronts are separated from each other by a wavelength λ with the aim to test if the dispersion relation (1) holds. We see that experimental lines of maximal amplitudes coincide perfectly with these curves, indicating that the predicted value of λ agrees with observations. In addition we have also drawn the two caustics. From a visual inspection of these figures, we can observe that the actual form of wave fields for small forcing amplitudes agree very well with geometrical optics predictions. Indeed, and as expected, for small amplitudes the nonlinear effects are negligible, meaning that the linear theory is appropriate to describe the wave fields. To get a better picture of the wave profiles, we present in Fig. 3 graphs of η as a function of y along the symmetry axis ($x = 0$) and for the two frequencies already considered. As can be seen, both curves are symmetric versus $\eta = 0$, meaning that crests and troughs are symmetric, attesting the absence of nonlinear effects. In addition, we can also observe that the amplitudes grow by a factor between 3.5 and 4.25, from the wave maker ($y = 0$) until a point located between 25 cm and 30 cm. As we will see later, this amplification factor stays around 4 in the different experiments we

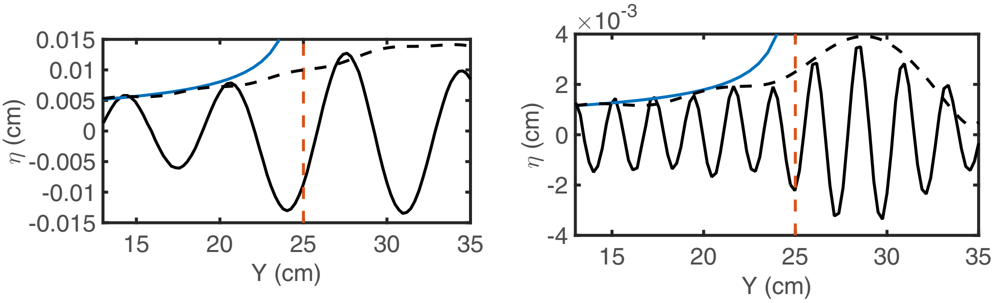

(a) (b)

FIG. 3. Deformation of the free surface η versus y along the symmetry axis ($x = 0$). (a) $f = 5\,\text{Hz}$, wavelength $\lambda = 6.5$ cm, and initial amplitude $\eta_0 = 36\ \mu\text{m}$. (b) $f = 10$ Hz, wavelength $\lambda = 2.3$ cm and initial amplitude $\eta_0 = 8\ \mu\text{m}$. Both curves are symmetric with respect to $\eta = 0$, attesting that nonlinearities are weak. Waves travel from left to right. For comparison we include the prediction of the ray theory for the wave envelope as given by Eq. (5) (blue line), the Pearcey prediction for the wave envelope, calculated from Eq. (8) (black dashed line), and the position of the Huygens cusp $y = \frac{1}{2a}$ (vertical red dashed line). The crests of experimental waves at both frequencies agree with the prediction of the ray theory when $y < 20$ cm, but for larger y, the Pearcey integral gives a better approximation.

performed and is less than those obtained by Rapp and Melville [8] using temporal focusing. The aforementioned point of maximal amplitude is close to the position of the Huygens cusp, which is $y = \frac{1}{2a} = 25$ cm in our experiments. In Fig. 3 the Huygens cusp is indicated by a vertical red line. According to the ray theory, the wave amplitude goes to infinity in that point, whereas in Pearcey theory, the maximal amplitude is reached in the vicinity of it. The experimental data are in good agreement with the Pearcey predictions.

B. Medium amplitude wave experiments: Emergence of weak nonlinear effects

A question then comes up: When does the linear theory fail to work? To answer this question we recall the pioneering work of Stokes [18] where he deduced some results about surface waves of finite but small amplitude. At leading order the results of linear wave theory are recovered, for instance, the dispersion relation for gravity waves ($w^2 = gk$). At next order, he found that the height of elevations exceeds the depth of troughs. In his theory the deformation of the free surface is given as the sum of two trigonometric functions:

$$\eta(y) = a\cos(ky) + \frac{ka^2}{2}\cos(2ky). \tag{11}$$

According to this equation the derivative $\frac{\partial\eta}{\partial y}$ (which can be measured directly from the synthetic Schlieren method) is

$$\frac{\partial\eta}{\partial y} = -ka\sin(ky) - (ka)^2\sin(2ky). \tag{12}$$

In order to recover the behavior of the wave envelope, we need to calculate the maximum and minimum values of η. These are, respectively, $\eta_{\text{max}} = a(1 + \frac{ka}{2})$ and $\eta_{\text{min}} = -a(1 - \frac{ka}{2})$. From these two relations it appears that the wave exhibits an asymmetry in the vertical direction. As a consequence the positive branch of the envelope becomes different from the negative one (for the last one we take its absolute value). To detect this asymmetry it is necessary that the difference (in absolute value) of positive and negative branches of the envelope (which is a^2k) becomes larger that the resolution of the synthetic Schlieren method. To estimate the resolution of the synthetic Schlieren

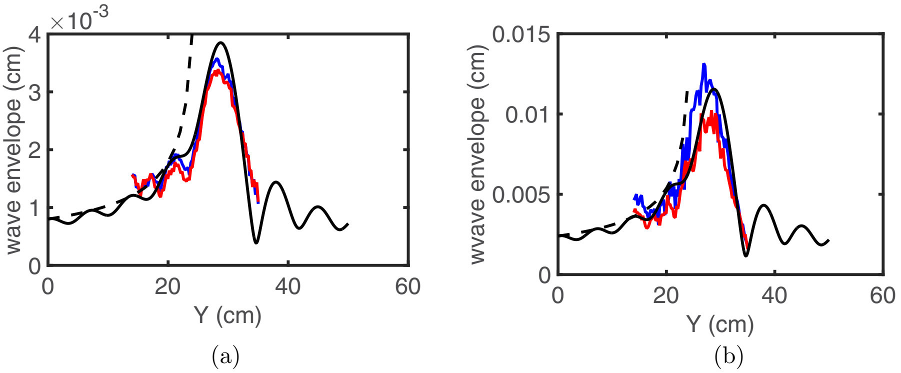

FIG. 4. Envelopes of η for a monochromatic wave of frequency $f = 10$ Hz. (a) Initial amplitude $\eta_0 = 8\ \mu$m. (b) Initial amplitude $\eta_0 = 24\ \mu$m. The blue curve is the positive branch of the envelope, whereas the red curve is the absolute value of the negative one. For comparison we include the predictions of the Pearcey integral (continuous black line) and the ray theory (dashed black lines). In the first case both branches of the envelopes remain close to each other, so nonlinear effects are undetectable. In the second case, the maximum difference between the two curves is approximately 10 μm, which is approximatively 2.5 times the prediction made by Stokes.

method we use the formula given by Moisy [15]:

$$\frac{\Delta\eta}{\eta_{rms}} \approx 5\frac{L\epsilon}{\lambda N}, \tag{13}$$

where L is the length of a side of the area covered by the image, N is the number of points in the grid, λ is the wavelength, and ϵ is the uncertainty of the input displacement field. In our measurements we use $L = 23$ cm and $N = 96$ and λ lies in the interval from 2.3 to 6.6 cm. In addition if we assume that the wave is nearly sinusoidal, $\eta_{rms} \approx \frac{a}{\sqrt{2}}$. In most experiments the resolution of η is $\Delta\eta \approx$ 1–2 μm, which is roughly the same as in the paper of Moisy [15]. Contrary to the behavior of the deformation η, the envelope of the derivative $\frac{\partial\eta}{\partial y}$ is symmetric in the Stokes theory. The envelopes of both η and $\frac{\partial\eta}{\partial y}$ were calculated following the evolution of waves in 1250 events. We have tested these predictions with monochromatic waves of various frequencies. For reasons of space in this paper we include only the results for the frequency of 10 Hz ($\lambda = 2.3$ cm) for two forcing amplitudes for the wave maker, $\eta_0 = 8\ \mu$m and $\eta_0 = 24\ \mu$m. In the first case the maximum amplitude is 34 μm, whereas in the second case the maximum amplitude is 110 μm. Taking these amplitudes as the value for a, the Stokes theory predicts that the maximum separation between the two branches of the envelope of η is, respectively, 0.3 μm and 4 μm. For the smaller amplitude the separation is less than our resolution, but in the second case not only the difference is greater than the resolution but it also represents about 4% of the wave amplitude. In Fig. 4 we present the two branches of the envelope of η (the positive branch is colored in blue, whereas the negative one is colored in red) for the two initial amplitudes mentioned before. With the aim to compare our results with the linear wave theory predictions, we include in the figure the prediction given by the Pearcey integral (the black line) and by the ray theory (the dashed line). For the smaller amplitude [Fig. 4(a)] both branches collapse on the complete interval. This result reflects that the nonlinear behavior remains undetectable here. On the contrary, the behavior is different for the larger amplitude $\eta_0 = 24\ \mu$m [see Fig. 4(b)]. In this case there is a clear difference between the two branches of the wave envelope. Maximum values are, respectively, 110 μm for the positive branch (blue line) and 100 μm for the negative one (red line). Then the difference between both branches is approximately 2.5 times the prediction of Stokes theory. This result is in accordance with Stokes theory in the sense that the crests are larger than troughs, but the theory underestimates the difference found in the experiment. This is probably due

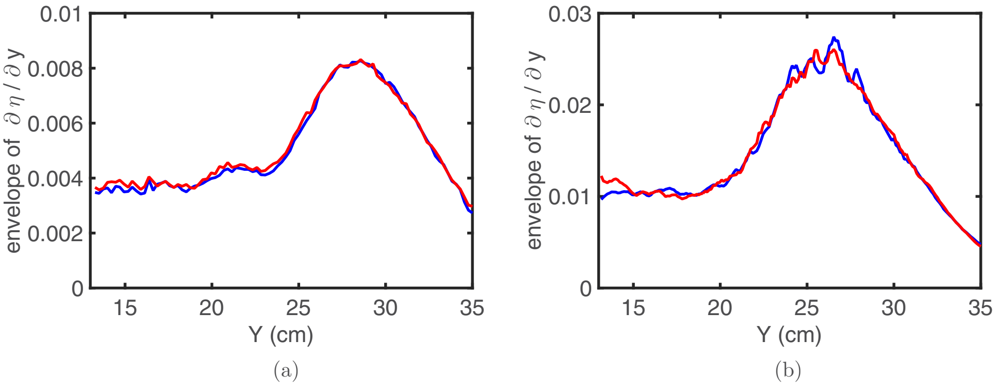

FIG. 5. Envelopes of $\frac{\partial \eta}{\partial y}$ for a monochromatic wave of frequency $f = 10\,\mathrm{Hz}$. (a) Initial amplitude $\eta_0 = 8\ \mu\mathrm{m}$. (b) Initial amplitude $\eta_0 = 24\ \mu\mathrm{m}$. The blue curve is the positive branch of the envelope, and the red curve is the negative one. For both cases positive and negative branches of envelope collapse, in agreement with the weak nonlinear theory by Stokes.

to the fact that the results of Stokes [18] are deduced for plane waves. As for the linear case studied in Sec. IV A, the predictions of linear waves and the ray theory are in an acceptable agreement with experimental data for $y < 20$ cm. In the vicinity of the Huygens cusp ($y = 25$ cm) the ray theory fails to predict correctly the wave behavior because it diverges at $y = \frac{1}{2a}$. On the contrary, the envelope calculated with the Pearcey integral agrees well with the experimental data. In Fig. 4(a), both experimental curves lie under the black curve, whereas in Fig. 4(b), the positive branch of the envelope is larger than the black line in the vicinity of the Huygens cusp. The comparison of positive (blue line) and negative (red line) of the envelope of $\frac{\partial \eta}{\partial y}$ are shown in Fig. 5. As predicted by Stokes theory, both branches collapse on one another in both cases.

C. Large amplitude wave experiments: Strong nonlinear effects

To test the possibility to increase more the amplitudes by focusing, we increased the forcing amplitude of the wave maker and thus of the generated waves. In these cases, the synthetic Schlieren method cannot be used any longer, and instead we use the FTP method. We choose a fringe pattern of periodicity $p = 2$ mm so that its spatial resolution (of the order of p) is much smaller than the features of interest and the minimum wavelength is $\lambda = 2.3$ cm. The topography of the free surface is measured in the region $-12\ \mathrm{cm} < x < 12$ cm and $5\ \mathrm{cm} < y < 35$ cm. In this subsection, we present some results for waves of frequency $f = 6.5$ Hz, and the corresponding wavelength given by the dispersion relation (1) is $\lambda = 4.2$ cm. We have chosen three different amplitudes to explore the regime of strong nonlinearity. The first case corresponds to an initial amplitude $\eta_0 = 200\ \mu\mathrm{m}$. In Fig. 6 we present both a wave profile along the symmetry axis and the topography of the free surface in the x-y plane. As expected, the wave amplitude grows on account of spatial focusing, and the wave develops a vertical asymmetry. The maximum amplitude of the crests is $\eta_{\max} = 0.074$ cm, whereas the maximum amplitude of the depressions is $\eta_{\min} = 0.062$ cm. In the preceding subsection the product ka was used to quantify the nonlinearity. If we consider these results, and assume that $a = (\eta_{\max} + \eta_{\min})/2$, then the maximum value of ka is now 0.1044, which is approximately three times those of the precedent subsection. Then we expect to have a more pronounced nonlinear behavior. According to Stokes theory the difference between the crests and the troughs should be $\Delta\eta = ka^2 = 0.0069$ cm. This value is less than the experimental result: $\eta_{\max} - \eta_{\min} = 0.012$ cm, by a factor 1.7. As before, we observe that if Stokes theory is able to detect the expected dissymmetry, it underestimates its amplitude in our case. Another insight in the wave behavior appears when we study the shape of the wave fronts. For this purpose in Fig. 6(b) we plot the topography of the free

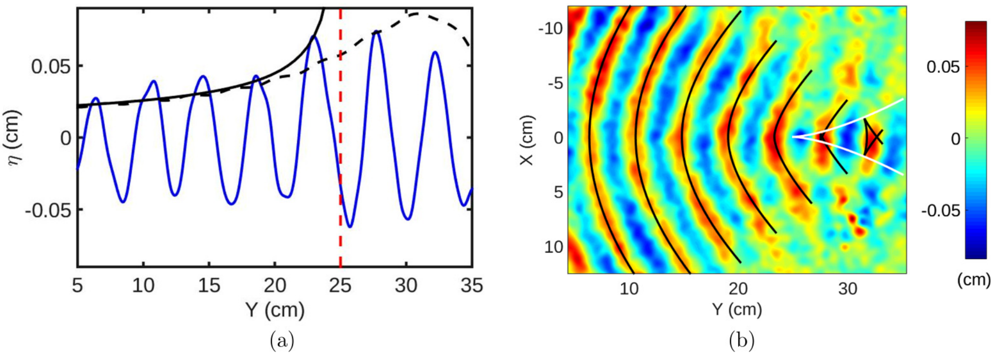

(a)

(b)

FIG. 6. (a) Wave profile η versus y along the symmetry axis (blue line) for a monochromatic wave of frequency $f = 6.5$ Hz and an initial amplitude $\eta_0 = 200\ \mu$m. For comparison we include the prediction of both the ray theory (continuous black line) and the Pearcey integral (black dashed line) for the envelope of the waves. The wave exhibits an asymmetry with respect to $\eta = 0$, which is a signature of a nonlinear behavior. In addition, wave crests are larger than the prediction of the wave envelope for $y < 20$ cm. (b) Topography of the free surface. For comparison we include some wave fronts as predicted from Eq. (3) (black lines) and the caustics (white lines). Despite the existence of a nonlinear behavior, there is still an agreement on the shape of the wave fronts between experiments and the ray theory prediction.

surface in the x-y plane. For comparison we include in the same figure some wave fronts as predicted by the ray theory (black curves). The visual agreement between theoretical and experimental data is satisfactory. Consequently, even if the nonlinearity is present for the results presented in Fig. 6, it is not strong enough to modify the shape of the wave fronts and their focusing.

When increasing the amplitude further, the wave field is highly modified. This can be seen in Fig. 7 where both the wave profile along the symmetry axis and the topography of the free surface

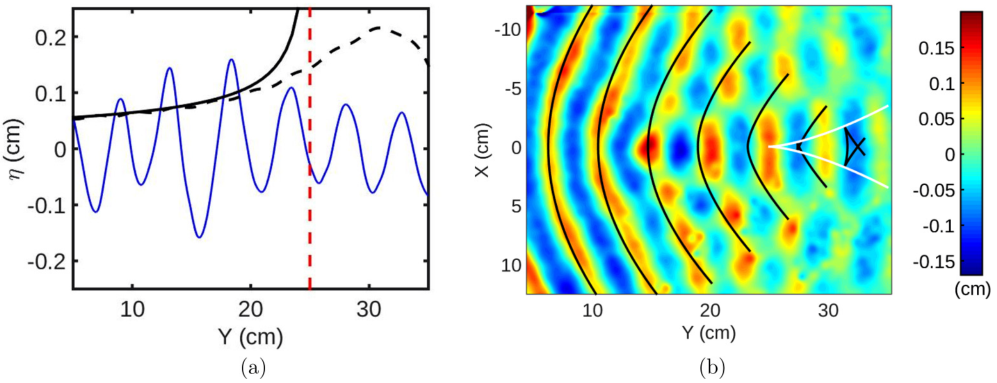

(a)

(b)

FIG. 7. (a) Wave profile versus y along the symmetry axis of a monochromatic wave of frequency $f = 6.5$ Hz and an initial amplitude $\eta_0 = 500\ \mu$m (blue line). For comparison we include the prediction of both the ray theory (continuous black line) and the Pearcey integral (black dashed line) for the wave's envelope. The wave profile is modified with respect to the case presented in Fig. 6. First, the position of maximal amplitude moves towards the wave maker. Second, the discrepancy between the amplitude of the crests and the envelopes is even greater. (b) Wave field in the domain $-12\,\text{cm} < x < 12$ cm and 5 cm $< y <$ 35 cm. For comparison, some wave fronts as predicted by the ray theory [deduced from Eq. (3)] are included (black lines) together with their corresponding caustics (white lines). The agreement with geometrical optics holds only near the plunger. Two differences emerge: first, the wavelength is no more equal to 4.2 cm, and, second, the wave fronts shape differs from the parabolic shape when moving away from the wave maker.

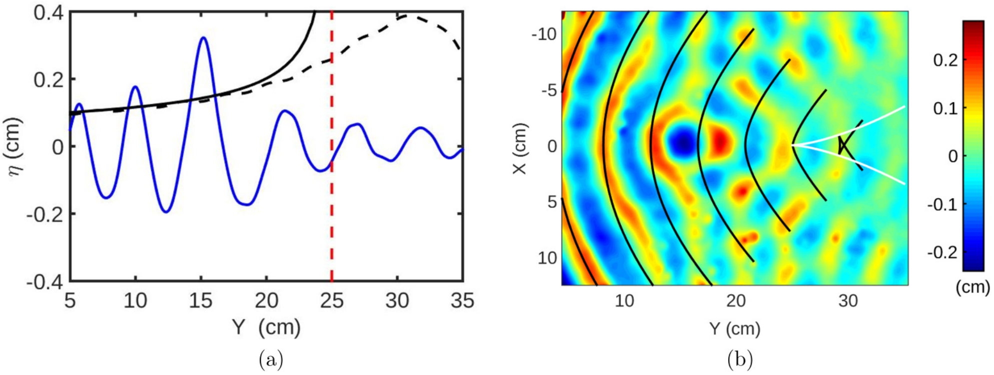

(a)

(b)

FIG. 8. (a) Wave profile versus y along the symmetry axis of a monochromatic wave of frequency $f = 6.5$ Hz and an initial amplitude $\eta_0 = 900$ μm (blue line). For comparison we include the prediction for the waves envelope of both the ray theory (continuous black line) and the Pearcey integral (black dashed line). The position of maximum amplitude stands approximately at $y = 15$. This point is closer to the wave maker than those obtained in the experiments with initial amplitudes $\eta_0 = 200$ μm and $\eta_0 = 500$ μm. (b) Wave field in the domain -12 cm $< x <$ 12 cm and 5 cm $< y <$ 35 cm. For comparison, some wave fronts as predicted by the ray theory [deduced from Eq. (3)] (black lines) and the caustics (white lines) are included. The wave field is very different to the prediction from geometrical optics.

are plotted for a wave of initial amplitude $\eta_0 = 500$ μm. First, Fig. 7(a) shows that the maximum amplitude happens in a point near $y = 20$ cm, which is not in agreement with the ray theory. Second, in Fig. 7(b) we plot the topography of the free surface, and we observe that the wave fronts exhibit differences with the ray theory as the wave goes away from the wave maker. For this amplitude, the agreement between ray theory and experiments holds only for the first period. For the remaining wave fronts, the differences occur in two respects: first, the distance between two successive crests for the experimental data is larger than the expected wavelength of 4.2 cm. Second, the curvature of the second and third wave fronts increases near the symmetry axis, enhancing the focusing. On the contrary, the fourth wave front corresponds to a diverging wave. At this position ($y \approx 20$ cm) the ray theory predicts that the wave fronts should still be convergent. Conversely, the curvature of experimental wave fronts on the side of the pattern (top and bottom of the figure) are smaller than the corresponding theoretical ones. A further increase of the initial amplitude makes even more evident these modifications. This can be seen in Fig. 8, where we present the wave profile along the symmetry axis and the topography of the free surface for an initial amplitude $\eta_0 = 900$ μm. The wave profile shown in Fig. 8(a) has a maximum amplitude located at $y = 15$ cm, very far from the expected 25 cm. After this point the wave amplitude decreases, which is a signature that the waves become divergent. As a consequence, Fig. 8(b) shows some important differences between experimental results and the prediction of ray theory (black lines). As in the previous figure, near the symmetry axis the curvature of the second and third experimental wave fronts is greater than the prediction of the ray theory. This behavior leads to a more pronounced focusing (from now we will call it “super” focusing), and therefore the point where curvature of wave fronts changes sign is close to $y = 15$ cm, a position which is 40% closer to the wave maker as compared to its position obtained with small amplitude waves [see Fig. 6(b)].

The results shown in Figs. 7 and 8 raise the following question: What is the source of the observed change in the wave pattern? We have found that the responsible of this unexpected behavior is the emergence of an horizontal large-scale flow at the liquid-air interface. This flow modifies the propagation of the waves, promoting a “super” focalization. This large-scale flow is formed by two recirculating cells and two jets situated on both sides of the symmetry axis of the wave maker. These cells play a major role in the properties of the wave field. The presence of the large-scale flow was detected by tracking small polystyrene particles on the free surface. These polystyrene

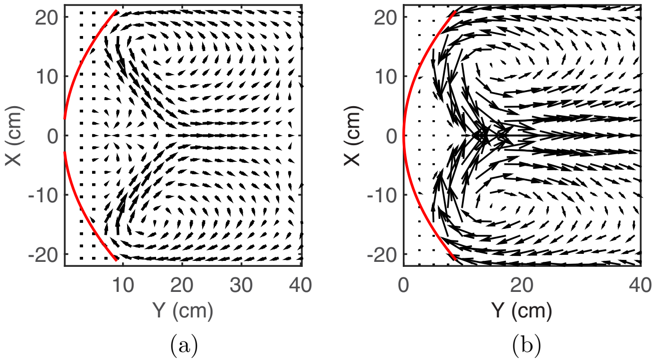

FIG. 9. Large-scale velocity field produced by a monochromatic wave of frequency $f = 6.5$ Hz and two different initial amplitudes: (a) $\eta_0 = 500\ \mu$m and (b) $\eta_0 = 900\ \mu$m. These amplitudes are the same as those used for experiment shown in Figs. 7 and 8. The wave maker is drawn in red on the left. Two vortices and two jets appear, symmetrically located with respect to the center line. When measuring the vorticity field, it appears to be different from zero, which is in contrary to the assumptions made to deduce the Stokes drift.

particles (around 4 mm in diameter spheres) are spread on the liquid-air interface. They have been painted in black, and the liquid was colored in white in order to facilitate their detection by contrast with the surrounding fluid. Initially the particles were uniformly distributed on the liquid surface with the aim to get data of the velocity field on all the domain. The positions of the particles were measured by taking images of the free surface at a rate of 25 frames/s with a full high-definition video camera (1920 × 1080 pixels) during 2 min, giving 3000 frames for each experiment. The position of individual particles are then tracked in all frames, and the velocity fields are deduced by differentiating the positions of each individual particle. The domain covers an area of 44 cm × 40 cm containing the wave maker and a region where wave evolves. To measure the velocity of the particles, the domain is divided in squares of 16 × 16 pixels (the corresponding length of a side of the square is 7 mm). When a particle reaches a cell, its velocity is assigned to the center of that cell. Finally the value of the velocity assigned to each square is the mean of the velocities of all the particles reaching the cell. In Fig. 9 we show the velocity field in the x-y plane corresponding to a wave of frequency $f = 6.5$ Hz and two different initial amplitudes $\eta_0 = 500\ \mu$m and $\eta_0 = 900\ \mu$m, that is, the same amplitudes as the waves presented in Figs. 7 and 8. In Fig. 9(a), which corresponds to an initial amplitude of $\eta_0 = 500\ \mu$m, the centers of the recirculating cells are located, respectively, at positions (15 cm, 16 cm) and (−15 cm, 16 cm). When the amplitude is $\eta_0 = 900\ \mu$m [see Fig. 9(b)] the cell centers are located at (12 cm, 15 cm) and (−12 cm, 15 cm). In general when increasing the wave amplitude the vortices approach to the wave maker. At the same time the direction of the jets is modified by a change of initial amplitude η_0. The larger is the wave amplitude, the larger is the transversal component (along the x direction) of the velocity inside the jets. The points where the jets are deflected and redirected along the y axis correspond roughly to the position of maximal wave amplitude. It is important to point out that when η_0 decreases, the flow weakens and we recover gradually the results of geometrical optics. Nevertheless, as the wave amplitude increases, the two jets act to modify the position of the maximal wave amplitude. When the amplitude rises from 500 μm up to 900 μm, the point of maximal amplitude moves from (0 cm, 20 cm) to (0 cm, 15 cm).

To estimate the modifications induced by the large-scale flow on the wave field, we proceed as follows. At the wave maker, the shape of the wave front is a parabola. As the wave moves away, we add the local velocity of the flow to the wave speed to calculate the new form of the wave front. This procedure allows us to modify the wave fronts taking into account the Doppler shift induced by the large-scale flow at the free surface. The main modifications of the wave fronts happen in the region where the two jets converge towards the symmetry axis. In Fig. 10 we draw the wave fronts resulting from the corrections induced by the velocity field (black lines) for a wave of frequency

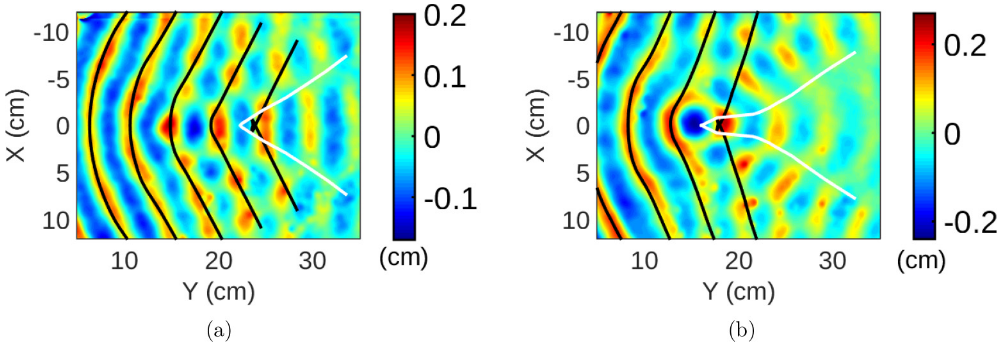

FIG. 10. Wave fronts in the presence of the large-scale flow. Black lines are the calculated wave fronts resulting from the transport induced by the large-scale velocity field. These wave fronts are superimposed to the experimental results and are in good agreement. (a) Wave field for $\eta = 500\ \mu$m and (b) wave field for $\eta = 900\ \mu$m. The presence of the large-scale flow modifies the shape of wave fronts. The Huygens cusp is located at $y = 21.5$ cm in the first case and at $y = 16$ cm in the second case. The resulting caustics are represented by the white lines.

$f = 6.5$ Hz and two initial amplitudes, $\eta_0 = 500\ \mu$m and $\eta_0 = 900\ \mu$m. For comparison we include the experimental data of the topography of the free surface. Finally, we have also included the two caustics (blue lines). The caustics have been obtained by using the property that they are the locations where wave fronts fold. As can be observed in Fig. 10, this Doppler shift argumentation fully explains why the waves have experienced a "super" focusing due to the jets converging towards the symmetry axis. This pushes away the Huygens cusp towards the left of the figure, i.e., closer to the wave maker. For the initial amplitude $\eta_0 = 500\ \mu$m this point is located at (0 cm, 21 cm), whereas for the wave of initial amplitude $\eta_0 = 900\ \mu$m the Huygens cusp is located at (0 cm, 16 cm).

The large-scale flow presented in Fig. 9 cannot be explained within the framework of the Stokes theory [18] because as we will see in the following, its intensity is not proportional to the square of the wave amplitude. A way to quantify the intensity of the flow is to determine the maximum values of the components (u, v) of its velocity field. The position where maximum values are attained is different for each of these components. For the transversal velocity u, its maximum value $u_{\max}$ happens along the jets, whereas for the longitudinal velocity v, its maximum value $(v_{\max})$ happens along the symmetry axis. In Fig. 11 we plot $u_{\max}$ versus the initial amplitude η_0 of the waves. As it can be seen in the figure, for small values of η_0, there is a linear relation between $u_{\max}$ and η_0. For larger

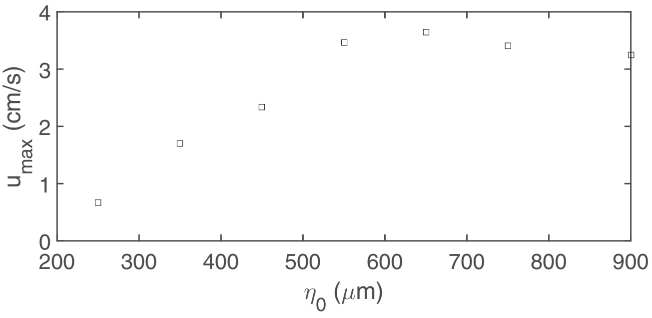

FIG. 11. Maximum value of the transversal component of the large-scale flow velocity field $u_{\max}$ as a function of the wave amplitude η_0. At weak wave amplitude, we observe a linear relation. However, $u_{\max}$ saturates for large values of η_0 and then slightly decreases. The overall behavior does not match with the Stokes drift but agrees with the results by Punzmann *et al.* [19].

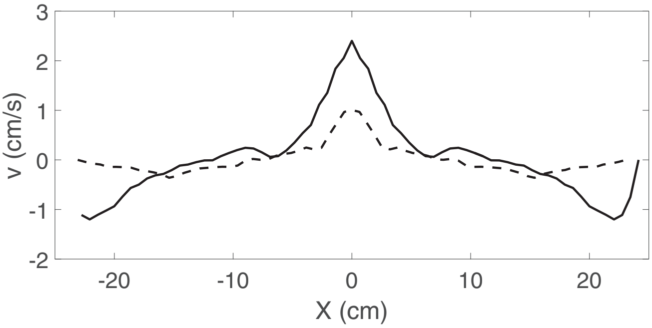

FIG. 12. Longitudinal velocity v profile along the x direction, for two different waves amplitudes, $\eta_0 = 250\ \mu\text{m}$ (continuous line) and $\eta_0 = 900\ \mu\text{m}$ (dashed line), for $y = 26.4$ cm and 20.2 cm, respectively. The maximum value of the velocity happens at the symmetry axis. We observe also negative values inside two intervals located symmetrically along the side of the container and corresponding to the back flow.

values of the wave amplitude, $u_{\max}$ saturates and even decreases. This behavior does not agree with the quadratic expected behavior of the Stokes drift but is close to the results obtained by Punzmann *et al.* [19]. The behavior of the v component of the velocity field is shown in Fig. 12, where we plot v as a function of x for two different values of the wave amplitude, $\eta_0 = 250\ \mu\text{m}$ and $\eta_0 = 900\ \mu\text{m}$. We have chosen to plot these profiles at the position where u reaches its maximal value ($y = 26.4$ cm and $y = 20.2$ cm, respectively). The maximum value of v happens at the symmetry axis ($x = 0$), and again the relation between $v_{\max}$ and η_0 is not quadratic. Besides, both curves show two intervals where v is negative, indicating that the velocity and the wave propagation are pointing in opposite direction. Another difference with Stokes drift theory is that the vorticity is nonzero, contrary to the assumption of a nonlinear potential theory of waves. In our experiments, we observe that the vorticity is concentrated in the two vortices and in the two jets. This can be seen in Fig. 13, where we have plotted the vorticity distribution in the x-y the plane for the two amplitudes considered here.

The appearance of this flow has been related to the boundary layer detachment of the liquid in contact with the wave maker as reported in recent papers. In particular, Punzmann *et al.* [19] present results of a flow produced by a plunger oscillating in the vertical direction. They found a large-scale flow composed of two or more vortices. To our understanding, a major role is played by the wave maker in the production of the large-scale flow. Of course, it produces the waves but its vertical

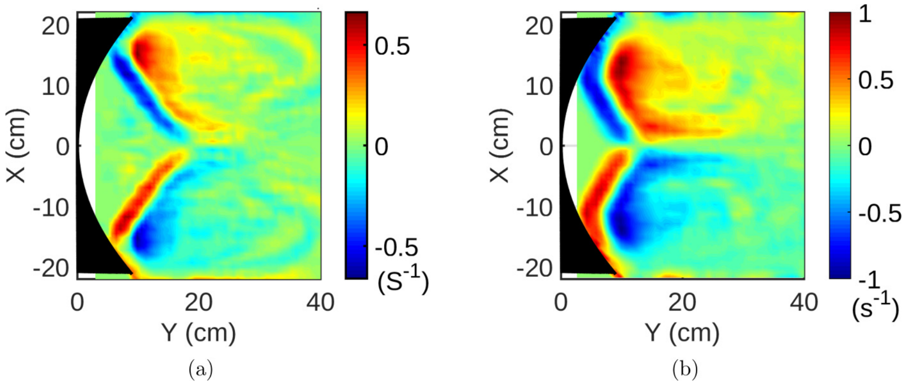

(a) (b)

FIG. 13. Vorticity distribution of the large-scale flow on the free surface. (a) Initial amplitude $\eta_0 = 500\ \mu\text{m}$ and (b) initial amplitude $\eta_0 = 900\ \mu\text{m}$. The vorticity is concentrated in the two recirculating cells and in the two jets. The flow is rotational, meaning that it does not fulfill the assumptions of the Stokes drift theory.

motion leads also to a horizontal displacement of the water because of mass conservation. Due to the nonslip boundary condition, the horizontal velocity of the fluid in contact with the wave maker falls to zero, and in consequence a boundary layer is formed. The boundary layer develops on both sides of the symmetry axis, producing a converging flow which moves away from the wave maker. The detachment of the boundary layer leads to the formation of two jets directed toward the symmetry axis. Because of the finite size of our container, the back flow is located along the lateral wall of the basin.

V. CONCLUSIONS

In this paper, the wave field produced by a parabolic wave maker has been investigated. Three regimes have been detected. In the first one, which corresponds to small amplitude waves, the experiments agree very well with the linear wave theory and with the ray theory. The wave profile is symmetric in the vertical direction, and maximal amplitude occurs near the Huygens cusp ($y =$ 25 cm). In the second regime, the nonlinearity is weak, but we can observe some effects associated to it. In particular, there is an asymmetry in the wave profile along the vertical direction. This implies that the amplitudes of the crests are larger than the amplitudes of the troughs. This behavior has been predicted by Stokes for plane waves, but for waves produced by a parabolic wave maker, the difference in amplitude between crests and troughs is larger than the difference predicted by Stokes theory. On the other hand, the shape of the wave fronts is not modified by the emergence of the nonlinearities, and wave focusing is still in accordance with the Pearcey integral prediction. Finally the third regime corresponds to a strong nonlinear behavior; a large-scale flow is superimposed on the wave field and modifies the shape of the wave fronts. In each point, the waves move with a speed which is the sum of the phase speed plus the local large-scale velocity field. This leads to a spatial “super” focusing where maximum amplitude is attained at a position closer to the wave maker by an amount as large as 40%. Nonetheless, in the three regimes, the spatial focusing technique leads to an amplification factor about four, slightly increasing with the wave frequency in accordance with the Pearcey integral, but lower than the growths observed in Ref. [8]. Note, however, that higher amplification rates and wave breaking can also be obtained by spatial focusing (of a single wave front) as performed by Tejerina and Le Gal, for instance [12]. In the third regime, we think that the emergence of the large-scale flow is related to the detachment of the boundary layer along the wave maker wall. Its nature is different from the Stokes drift in two respects: first, because its amplitude is not proportional to the square of the wave amplitude and, second, because the flow is rotational. Moreover, this large-scale flow that deforms the wave fronts might in consequence inhibit the breaking of the waves by limiting the growth of their slopes. This subject will deserve future analysis.

ACKNOWLEDGMENTS

We thank Eric Falcon from Paris Diderot University for his assistance in implementing the Fourier transform profilometry. We also acknowledge Sergio Hernandez Zapata for useful comments about this paper. This research was financed by DGAPA-UNAM, under contract PAPIIT IN-115315 “Vorticidad y estructuras coherentes en dinamica de fluidos,” and IRPHE of Aix Marseille University. G.R.C. was supported by a Sabbatical Fellowship at IRPHE by DGAPA-UNAM. P.L.G. thanks Aix Marseille Université for the fundings Appel à Projets Actions Internationales 2015 and 2016 and UNAM, Contract No. PAPIIT IN-115315.

---

[1] M. Perlin, W. Choi, and Z. Tian, Breaking waves in deep and intermediate waters, Annu. Rev. Fluid Mech. **45**, 115 (2013).

[2] L. Deike, W. Kendall Melville, and S. Popinet, Air entrainment and bubble statistics in breaking waves, J. Fluid Mech. **801**, 91 (2016).

[3] N. E. Pizzo, L. Deike, and W. Kendall Melville, Current generation by deep-water breaking waves, J. Fluid Mech. **803**, 275 (2016).

[4] A. Babanin, *Breaking and Dissipation of Surface Waves* (Cambridge University Press, Cambridge, 2011).

[5] J. Touboul and C. C. Kharif, Effects of vorticity on the generation of rogue waves due to dispersive focusing, Nat. Hazard **84** (Suppl. 2), 585 (2016).

[6] C. Fochesato, S. Grilli, and F. Dias, Numerical modeling of extreme rogue waves generated by directional energy focusing, Wave motion **44**, 395 (2007).

[7] M. S. Longuet-Higgins, Breaking waves—In deep or shallow waters, in *10th Symp. on Naval Hydrodynamics*, edited by Ralph D. Cooper and Stanley W. Doroff (Office of Naval Research, Department of Navy, Arlington, VA, 1974), p. 597.

[8] R. J. Rapp and W. K. Melville, Laboratory experiments of deep-water breaking waves, Phil. Trans. R. Soc. Lond. A **331**, 735 (1990).

[9] K. She, C. A. Greated, and W. J. Easson, Experimental study of three-dimensional breaking wave kinematics, Appl. Ocean Res. **19**, 329 (1997).

[10] Y. Pomeau, Caustics of nonlinear waves and related questions, Europhys. Lett. **11**, 713 (1990).

[11] I. Pearcey, The structure of an electromagnetic field in the neighborhood of a cusp of a caustic, Phylos. Mag. **37**, 311 (1946).

[12] J. Tejerina-Risso and P. Le Gal, Around the cusp singularity and the breaking of waves, Leonardo **47**, 80 (2014).

[13] G. Ruiz Chavarria, P. Le Gal, M. Le Bars, and Y. Pomeau, Focalisation d'ondes de surface et déferlement, in *Actes du XXe Congrès Français de Mécanique*, edited by P. Picart, D. Chapelle, and M. Dahan (Presses Universitaires de la Franche-Comté, Besançon, France, 2012), p. 775.

[14] G. B. Airy, On the intensity of light in the neighbourhoud of a caustic, Trans. Cambridge Philos. Soc. **6**, 379 (1838).

[15] F. Moisy, M. Rabaud, and K. Salsac, A synthetic Schlieren method for the measurement of the topography of a liquid surface, Exp. Fluids **46**, 1021 (2009).

[16] P. J. Cobelli, A. Maurel, V. Pagneux, and P. Petitjeans, Global measurement of water waves by Fourier transform profilometry, Exp. Fluids **46**, 1037 (2009).

[17] P. Meunier and T. Leweke, Analysis and minimization of errors due to high gradients in particle image velocimetry, Exp. Fluids **35**, 408 (2003).

[18] G. Stokes, On the theory of the oscillatory waves, Trans. Cambridge Philos. Soc. **8**, 441 (1847).

[19] H. Punzmann, N. Francois, H. Xia, G. Falcovich, and M. Shats, Generation and reversal of surface flows by propagating waves, Nat. Phys. **10**, 658 (2014).